Transactions of Materials Research 1 (2025) 100013

Contents lists available at ScienceDirect

Transactions of Materials Research

journal homepage: www.sciencedirect.com/journal/transactions-of-materials-research

Li/Na storage enhancement of MoS_2 particles through surface electronic structure adjustment

Ning Zhang [a], Yuetong Li [a], Botao Zhang [a], Shengyu Gao [a], Yongxin Huang [a,b,*], Li Li [a,b,c], Feng Wu [a,b,c], Renjie Chen [a,b,c]

[a] Beijing Key Laboratory of Environmental Science and Engineering, School of Material Science & Engineering, Beijing Institute of Technology, Beijing, 100081, China
[b] Innovative Research Team in High-Safety Energy Storage System and Smart Microgrids of Guangdong Province, Beijing Institute of Technology (Zhuhai), Zhuhai, 519088, China
[c] Collaborative Innovation Center of Electric Vehicles in Beijing, Beijing, 100081, China

ARTICLE INFO

Keywords:
Li/Na storage
MoS_2 anode
Derived N-doped carbon
Surface electronic structure adjustment

ABSTRACT

Commercialization of MoS_2 electrode materials has been severely limited due to low electrical conductivity and significant volume variations during their cycling. Meanwhile, bottom-up modification strategies require precise experimental conditions and control techniques, which further restrict the industrial application of MoS_2 materials. Herein, the changes in the electronic structure of MoS_2 surfaces due to carbon coating and N-doped carbon coating are compared through theoretical calculations. Based on this, a top-down modification strategy is proposed, involving mechanical pulverization and N-doped carbon layer coating of commercial MoS_2 through high-energy ball milling and ultrasound-assisted *in situ* coating technology, and carbonization. This strategy effectively improves the electronic structure of the surface of MoS_2 particles, enhancing the ion transport kinetics and cycling stability of molybdenum disulfide. Thanks to the elemental and structural advantages, the coated MoS_2 exhibits excellent electrochemical performance, with outstanding specific capacity and cyclic stability (specific capacity of 753.9 mAh g^{-1} at a current density of 500 mA g^{-1} after 200 cycles, with a capacity retention percentage of 92.2 %) as well as excellent rate performance (specific capacity of 302.9 mAh g^{-1} after 500 cycles at a current density of 5 A g^{-1}). This study not only establishes a detailed scheme for enhancing the lithium storage performance of MoS_2 but also provides new insights for its industrial research.

1. Introduction

Lithium-ion batteries (LIBs), with advantages such as high energy density, long lifespan, low self-discharge rate, and absence of memory effect, have become the primary power source for various electronic devices and transportation such as phones, computers, and electric vehicles [1–3]. Over the past few decades, extensive material research has been conducted on each component of LIBs to enhance their electrochemical performance. In fact, graphite is the mainstream negative electrode material for LIBs, but its theoretical specific capacity is relatively low (372 mAh g^{-1}), no longer meeting the trend of high energy density storage power development [4,5]. Consequently, various materials with high theoretical specific capacities have been investigated to replace graphite anodes. For example, silicon has a high lithium storage theoretical specific capacity of 4200 mAh g^{-1}, but its application is severely limited by the significant volume expansion during lithium storage and the cycle stability issues because of chemical reactions with lithium. The high specific capacity (3860 mAh g^{-1}) and low electrode potential of lithium metal electrodes make them promising anode materials for lithium-ion batteries, but safety and cyclic stability issues arising from dendrite growth, corrosion, and volume changes during operation have hindered their applications [6,7]. Conversion-type negative electrode materials (transition metal oxides, transition metal sulfides, and transition metal phosphides) are considered as alternative materials to carbon materials due to their higher specific capacity. Among other conversion negative electrode materials, transition metal sulfides (TMSs) have higher theoretical specific capacities, conductivity, and thermal stability. Additionally, the voltage platform of TMSs is usually above 1.0 V, which avoids lithium dendrite formation during cycling for high safety [8].

* Corresponding author. Beijing Key Laboratory of Environmental Science and Engineering, School of Material Science & Engineering, Beijing Institute of Technology, Beijing, 100081, China.
E-mail address: huangyx@bit.edu.cn (Y. Huang).

https://doi.org/10.1016/j.tramat.2025.100013
Received 21 March 2025; Received in revised form 7 April 2025; Accepted 7 April 2025
Available online 8 April 2025
3050-9149/© 2025 The Authors. Published by Elsevier B.V. on behalf of Chinese Materials Research Society. This is an open access article under the CC BY license (http://creativecommons.org/licenses/by/4.0/).

As a representative transition metal sulfide, MoS_2 offers several advantages, including abundant reserves, a wide range of applications, and suitable gravimetric and volumetric energy densities (Fig. 1). However, as an anode material for LIBs, MoS_2 has not achieved successful commercialization mainly due to the following issues [8–10]: (1) Low intrinsic electronic and ionic conductivities, leading to sluggish lithium-ion diffusion kinetics, which results in low specific capacity and poor rate performance. (2) Severe volume expansion and contraction during charge and discharge cycles, which can easily cause material agglomeration and structural collapse, especially under high current densities. To address these issues, various modification strategies have been proposed to enhance the electrochemical performance of MoS_2, including the preparation of nanomaterials with unique morphologies, expanding interlayer spacing, 1T phase transition, and compositing with conductive buffering materials [11]. Among various modification techniques, nano-miniaturization and carbon coating technologies have garnered widespread attention due to their simplicity and significant effects. In particular, carbon coating can alter the electronic structure of the material's surface, thereby promoting the absorption of Li^+, which in turn accelerates the reaction kinetics [12]. Meanwhile, the N-doping effect can control the carrier density, surface energy, and electron gain and loss capabilities by regulating the internal defects and electronic states of carbon materials. There are various configurations of N-doping, such as graphitic nitrogen, edge pyridinic nitrogen, pyridinic nitrogen at single vacancies, porphyrin nitrogen, and pyrrolic nitrogen. Due to the differences in defects and electronic structures, the doping of different configurations has significant impacts on many properties of carbon materials [13].

Therefore, the density of states, adsorption energies, and charge densities of commonly encountered nitrogen-doped carbon layers with different configurations were studied through theoretical calculations. Based on this, various configurations of N-doped carbon layers were prepared, and the modification effects on commercial MoS_2 particles were experimentally verified. Firstly, nano-scale bulk particles were obtained from commercial bulk MoS_2 particles through a ball-milling mechanical grinding process. Subsequently, an unsaturated conjugated Schiff base macromolecule with alternating benzene rings and C=N linkages was *in situ* coated onto the particles via the reaction of p-phenylenediamine and terephthalaldehyde in ethanol. Finally, a carbonization process yielded MoS_2@C(N) composites, where MoS_2 bulk particles were coated with a thin N-doped carbon shell. The porous structure of the N-doped carbon facilitates good contact between the composite material and the electrolyte, while buffering the significant volume changes of MoS_2 during lithiation/de-lithiation. Additionally, the introduction of the carbon structure effectively prevents the agglomeration of MoS_2 nanoparticles during charge-discharge cycles, ensuring structural stability. It is noteworthy that the *in situ* reaction coating with Schiff base molecules results in a uniform distribution of N in the carbon layer, effectively preventing the dissolution of Li_2S in the electrolyte, which is crucial for the capacity retention of MoS_2 active particles. The simplicity of the procedure and the abundance of commercial MoS_2 resources make this approach more promising for preparations of commercial electrode materials.

Benefiting from the dual effects of elemental and structural modifications, the resulting MoS_2@C(N) composite material exhibits excellent lithium storage performance. At a current density of 500 mA g^{-1}, it delivers a specific capacity of 753.9 mAh g^{-1} after 200 cycles, with a capacity retention rate of 92.2 %, showing a significant improvement

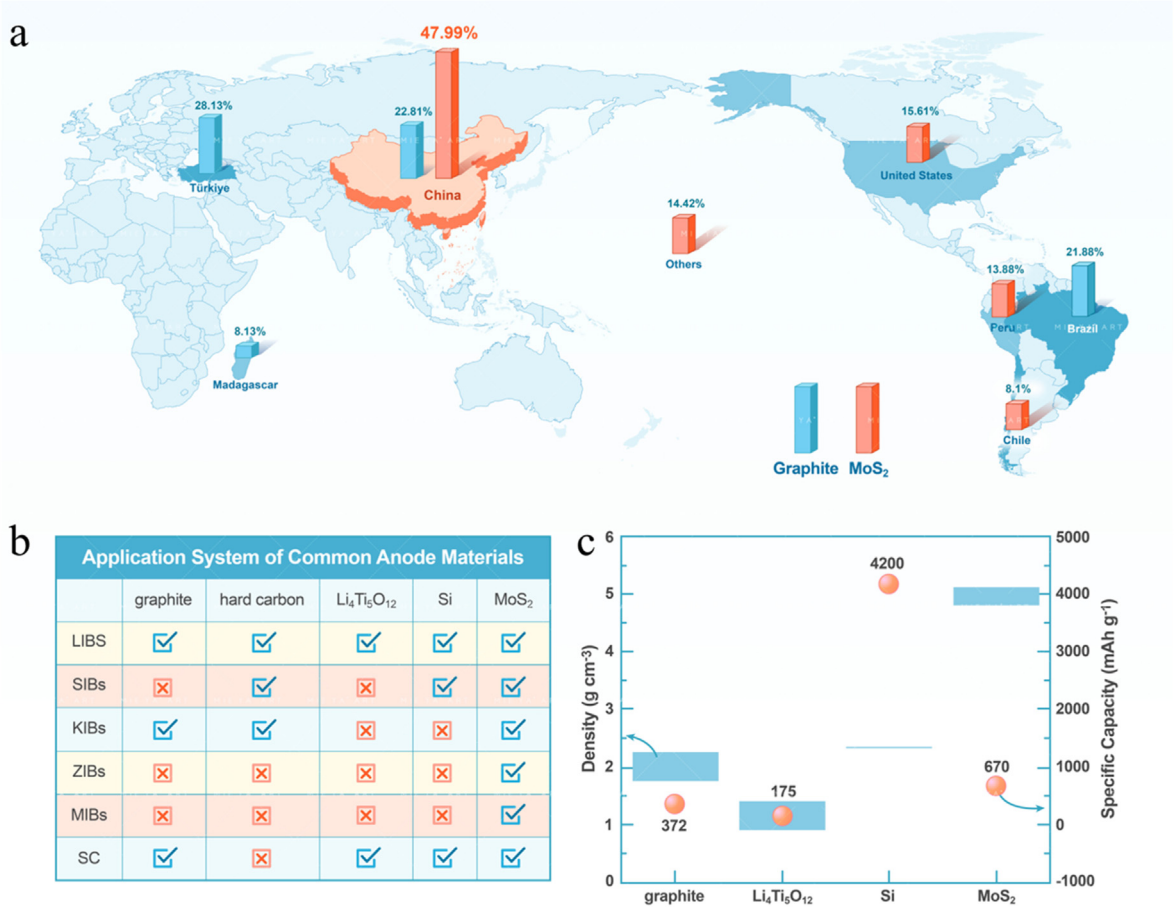

Fig. 1. (a) Proportion of MoS_2 and graphite reserved in China [the data are sourced from the United States Geological Survey (USGS)]. (b) Energy storage systems applicable for common anode materials. (c) Gravimetric density and theoretical energy density of conventional electrode materials.

compared to nano-sized particles directly obtained from commercial MoS_2. Additionally, at a high current density of 5 A g^{-1}, the composite maintains a specific capacity of 302.9 mAh g^{-1} even after 500 charge-discharge cycles, demonstrating exceptional rate performance and cycling stability, indicating its broad potential for practical applications.

2. Experimental section

2.1. Synthesis of materials

Commercial MoS_2 material was ball-milled for 30 min to further reduce its particle size. Then, 2-g ball-milled MoS_2 was dispersed in 20 ml of anhydrous ethanol to obtain solution I. Next, 0.649-g (6 mmol) p-phenylenediamine was dissolved in 20 ml of anhydrous ethanol to obtain solution II, and 0.877 g (6 mmol) of terephthalaldehyde was dissolved in 20 ml of anhydrous ethanol to obtain solution III. Solutions II and III were then added dropwise to solution I under ultrasonic conditions. After the addition was complete, the mixture was sonicated for an additional 30 min to obtain a solid precipitate, which was washed with anhydrous ethanol more than three times. The solid was then dried in an oven at 60 °C to yield a black solid powder. The dried solid powder was placed in an alumina boat and annealed in an inert atmosphere (Ar) at a heating rate of 5 °C min^{-1}, heated to 700 °C, maintained for 2 h, and then naturally cooled to room temperature to obtain the nitrogen-doped carbon-coated MoS_2 composite nanomaterial.

2.2. Materials characterization

The morphologies of the as-synthesized samples were characterized with SEM (FEI XL30 Sirion) at an accelerating voltage of 10 kV. The microstructures of the products were determined by TEM (FEI Tecnai G2 F30). EDS elemental maps were used to define the distribution of elements. X-ray powder diffraction (XRD, Bruker D8 Advance) with Cu K_α radiation range from 5° to 60° and Raman spectroscopy (LabRAM HR Evolution, France) were employed to investigate the structure and crystalline phases by using a 532 nm laser source. The chemical composition of all the samples was collected by an X-ray photoelectron spectroscope (XPS, Thermo Scientific K-Alpha+, USA) using Al K_α radiation. Furthermore, all the DFT calculations were conducted based on the Vienna *ab inito* simulation package (VASP). The Perdew-Burke-Ernzerhof (PBE) functional within the generalized gradient approximation (GGA) method was adopted to describe the exchange-correlation effects. The projected augmented wave (PAW) method accounted the core-valence interactions. The energy cutoff for plane wave expansions was set to 400 eV. The structural optimization was completed for energy and force convergence set at 1.0×10^{-4} eV and 0.05 eV $Å^{-1}$, respectively. The Brillouin zone was sampled with the $3 \times 3 \times 1$ *K*-point (when calculating the adsorption energy of LiS_2 in carbon layer, the Brillouin zone was sampled with the $1 \times 1 \times 1$ *K*-point). Grimme's DFT-D3 methodology was used to describe the dispersion interactions.

The adsorption energy (E_{ads}) of Li is calculated by

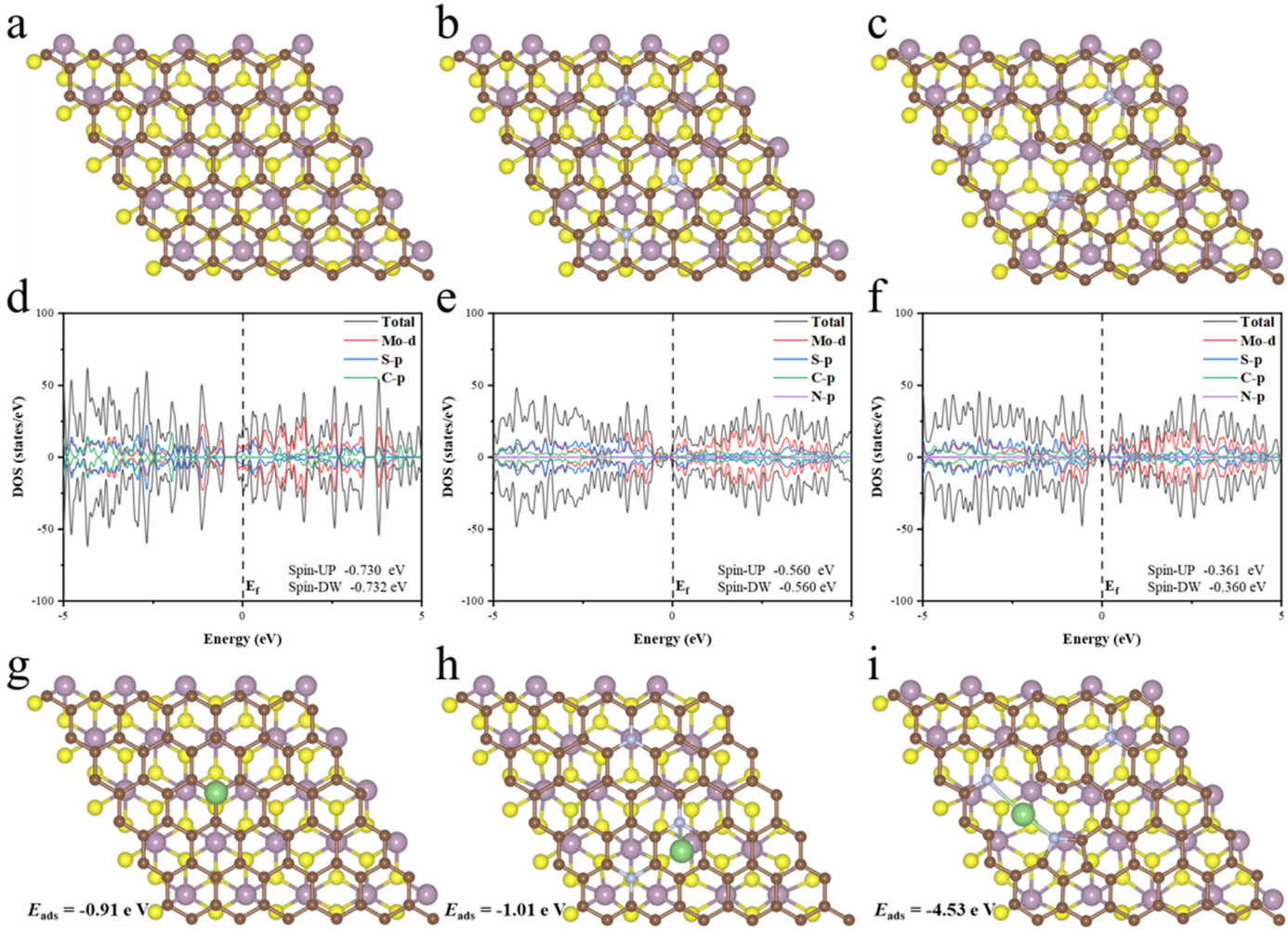

Fig. 2. (a–c) Top views, (d–f) density of states, and (g–i) adsorption energies of three models: MoS_2@C, MoS_2@C (Graphitic N), and MoS_2@C (Graphitic N/Pyridine N/Pyrrole N).

$$E_{ads} = E^{*}_{Li} - E_{Li} - E_{sub}$$

where E^{*}_{Li} represents the energy after the adsorption of Li on the substrates. E_{Li} is the energy of the Li single atom. E_{sub} is the energy of C-MoS_2 and CN-MoS_2 surfaces. Meanwhile, the adsorption energy (E_{ads}) of Li_2S is calculated with the similar method.

2.3. Electrochemical measurements

The battery assembly was carried out in an Ar-filled glovebox (Mikrouna, Germany, $H_2O \leq 0.1$ ppm, $O_2 \leq 0.1$ ppm), and 2025-type coin cells were used to study the electrochemical properties. A Celgard 2400 membrane served as separator, 1:1 organic solvent mixture by volume of ethylene carbonate, diethyl carbonate (EC:DEC) with 1 M $LiPF_6$ as electrolyte, and lithium foil as the counter electrode. The as-prepared materials were kept in vacuum oven for overnight at 100 °C before making electrode slurry. For the half-cell testing, the working electrode was prepared by thoroughly mixing the 80 wt% as-synthesized material, 10 wt% polyvinylidene fluoride (PVDF), and 10 wt% acetylene black (Super P) in N-methylpyrrolidone (NMP) with vigorous stirring for 12 h, which was coated on copper foil and vacuum dried at 100 °C for 12 h. Furthermore, the galvanostatic charge/discharge cycling test in the voltage window of 0.1–3 V was conducted on Neware Test System (Neware CT-5000, China) at various current densities. The coin cells were assembled by the traditional method. Cyclic voltammetry (CV) curves were obtained on an electrochemical workstation (CHI760E, China) in the range from 0.01 to 3 V. Electrochemical impedance spectroscopy was recorded on an electrochemical workstation over the frequency range from 0.01 Hz to 100 kHz. The current densities and capacities were calculated based on the weight of the entire electrode.

3. Results and discussion

The modulation of electronic structures is investigated using DFT calculations. Initially, the optimized structures of three models, MoS_2@C, MoS_2@C (Graphitic N), and MoS_2@C (Graphitic N/Pyridine N/Pyrrole N), are proposed, as shown in Fig. 2a–c. Fig. 2d–f displays the total and partial density of states (TDOS and PDOS) near the Fermi level for three models. It was clearly observed that VB below the Fermi level was formed by every elemental orbital whereas CB above the Fermi level was majorly formed by Mo 4*d* orbital. The presence of N 2*p* orbital leads to greater overlap of the electronic state density around the Fermi level, resulting in higher charge transfer and conductivity characteristics. N-doping, especially the introduction of pyridine N and pyrrole N, can effectively reduce the bandgap of the material, achieve higher electrical conductivity, and enhance electron transfer kinetics [14,15]. As shown in Fig. 2g–i, all of the three kinds of materials exhibit the negative values, indicating that the carbon layers facilitate the absorption of Na^{+}, which can fasten the reaction kinetics. However, the introduction of pyridine N and pyrrole N can effectively enhance the effect [13].

Although the introduction of N elements enhances the affinity of the carbon layer for Li, it often leads to the transfer of interfacial charge from MoS_2 to the carbon matrix, thereby exacerbating its side reactions with the electrolyte and reducing the reactivity of MoS_2 [12]. According to the charge density difference (Fig. 3a–c), the introduction of graphitic N exhibits the strongest electron transfer phenomenon, while the introduction of pyridinic N and pyrrolic N is limited by the electron donor effect, restricting charge transfer. This allows the material to have high Li^{+} adsorption energy bands while exhibiting weaker side reactions and stronger MoS_2 reactivity. The plane-averaged charge density distribution curves (Fig. 3d–f) intuitively illustrate this phenomenon.

Inspired by the above DFT results, MoS_2@C (Graphitic N/Pyridine N/Pyrrole N) composite is designed based on commercial MoS_2 materials. Fig. 4 illustrates the steps of the preparation of the composite material. Firstly, commercial MoS_2 particles are dispersed into spheroid-like nanoparticles using dry ball milling technology and washed with ethanol solute on to remove soluble impurities remaining in the commercial preparation process. Then, under ultrasonic conditions in an ethanol solution, a conjugated Schiff base polymer is grown *in situ*, utilizing the coordination of imine bonds with Mo^{4+} to uniformly coat the nanoparticle surfaces [16]. This is followed by an annealing process under inert conditions to convert the polymer into nitrogen-doped carbon material, while a low-temperature pre-carbonization process is used to maintain its inherent porous structure. The final product is the

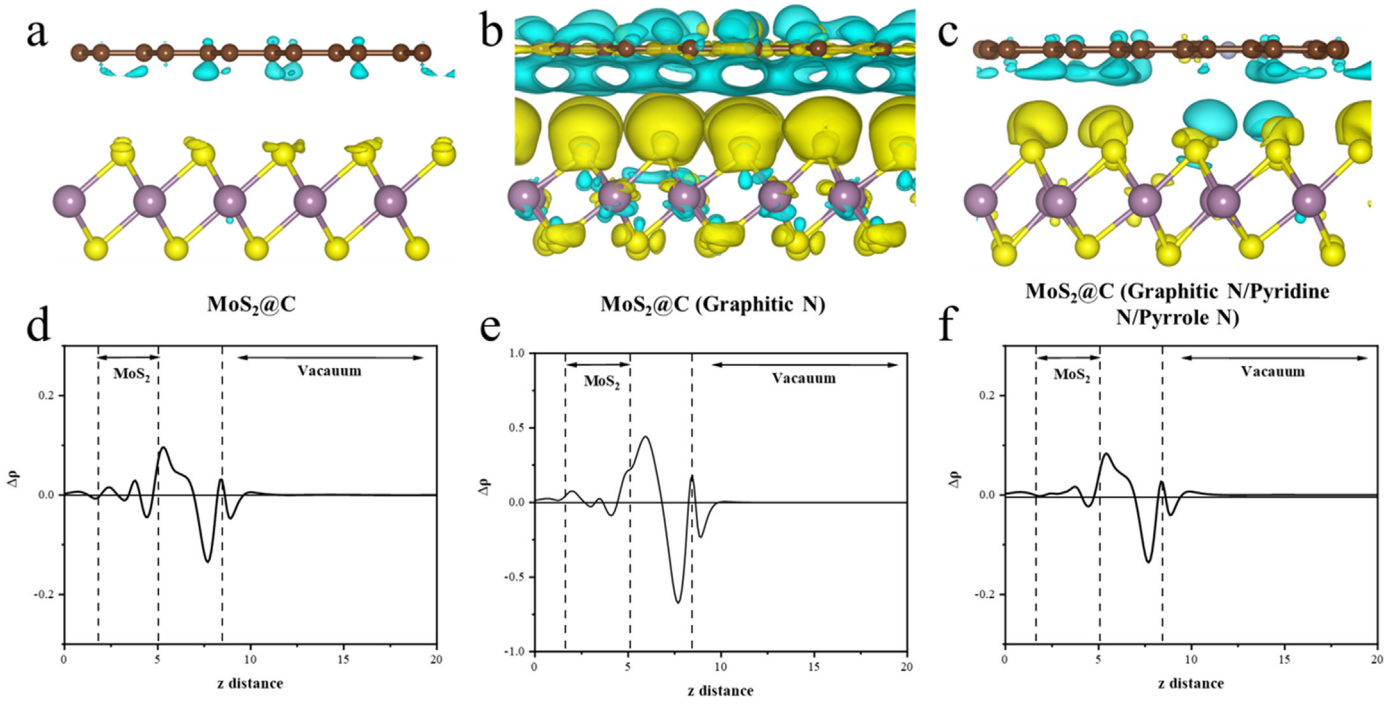

Fig. 3. (a–c) The charge density difference (yellow and cyan represent charge accumulation and depletion, respectively) and (d–f) plane-averaged charge density distribution curves of MoS_2@C, MoS_2@C (Graphitic N), and (c) MoS_2@C (Graphitic N/Pyridine N/Pyrrole N) models.

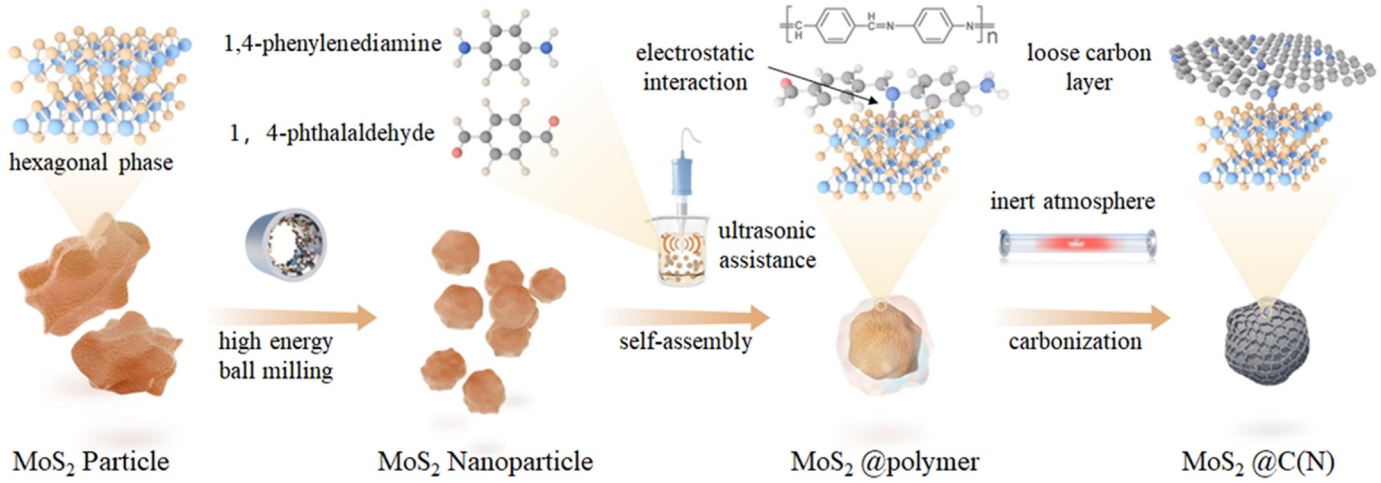

Fig. 4. Preparation steps of the MoS_2@C(N) material.

MoS_2@C(N) composite material with a uniformly coated nano-scale carbon layer.

Fig. 5a and b shows the SEM images of MoS_2 and MoS_2@C(N) composites at 1 μm (inset at 20 nm). Both MoS_2 and MoS_2@C(N) exhibit irregular particulate morphologies, but the N-doped carbon layer coating smooths the active edge surfaces, facilitating smoother Li^+ migration paths on the surface [17]. The EDS image of the MoS_2@C(N) powder, as shown in Fig. 5c, confirms the presence of Mo, S, C, and N elements. Notably, the uniform distribution of C and N elements in the selected area further demonstrates the uniformity of the coating. The TEM images (Fig. 5d and e) reveal the internal structure of MoS_2@C(N). An amorphous, porous N-doped carbon layer coats the surface of MoS_2. This porous structure ensures sufficient contact between the electrolyte and the active material, as well as high ionic conductivity, thereby enhancing the charge-discharge rate and efficiency of the electrode material. The presence of the carbon layer plays a crucial role in improving the electronic conductivity of the MoS_2 nanoparticles. The interface between the carbon layer and MoS_2 nanoparticles also provides additional pathways for Li^+ migration. The EDS spectrum from the TEM further illustrates the elemental distribution on the surface and interior of the sample (Fig. 5f).

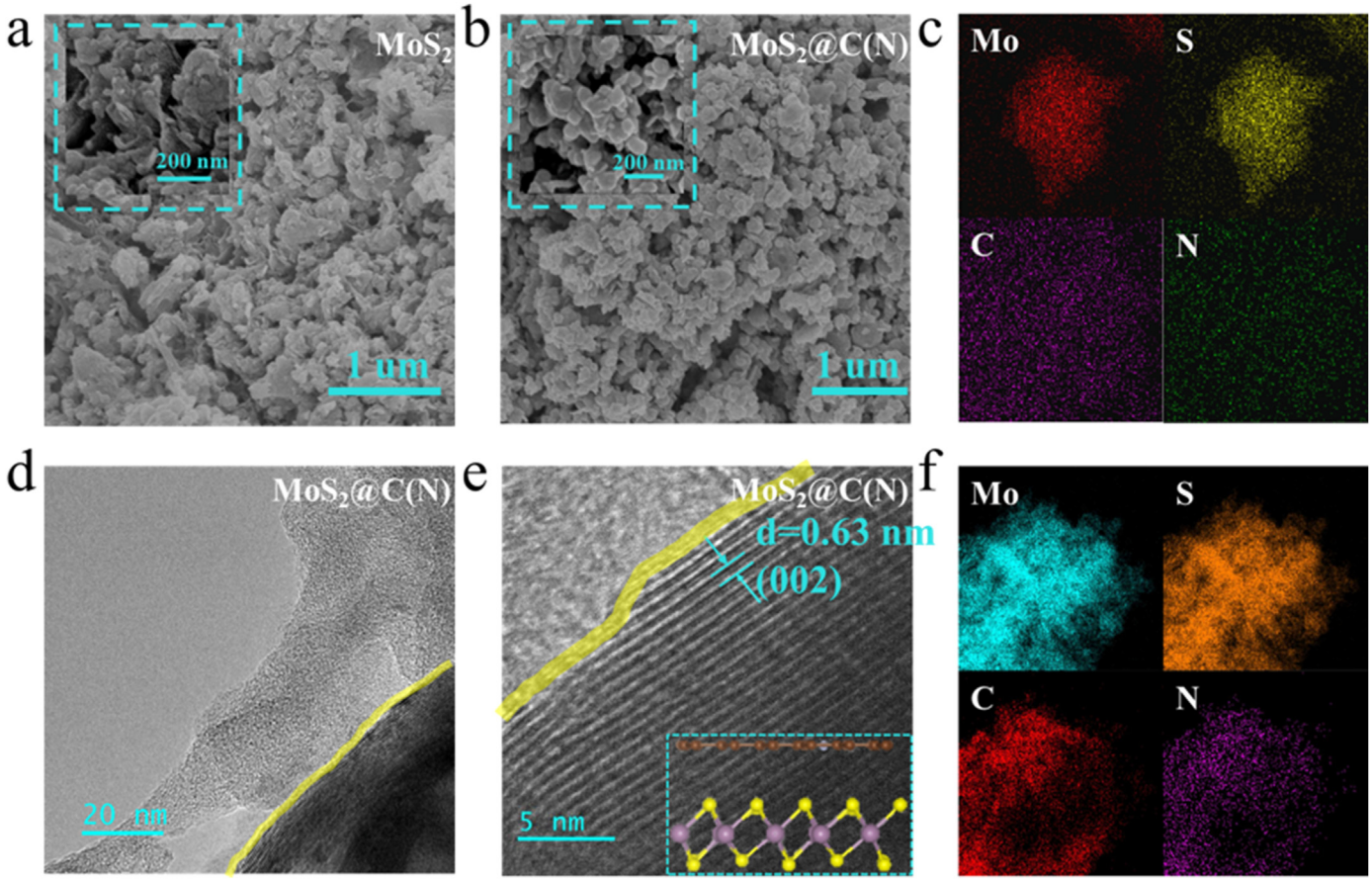

Fig. 5. (a, b) scanning electron microscope (SEM) images of MoS_2 and MoS_2@C(N) composites, (c) energy-dispersive spectroscopy (EDS) spectra, (d, e) transmission electron microscope (TEM) images of MoS_2 and MoS_2@C(N) composites, and (f) EDS spectra.

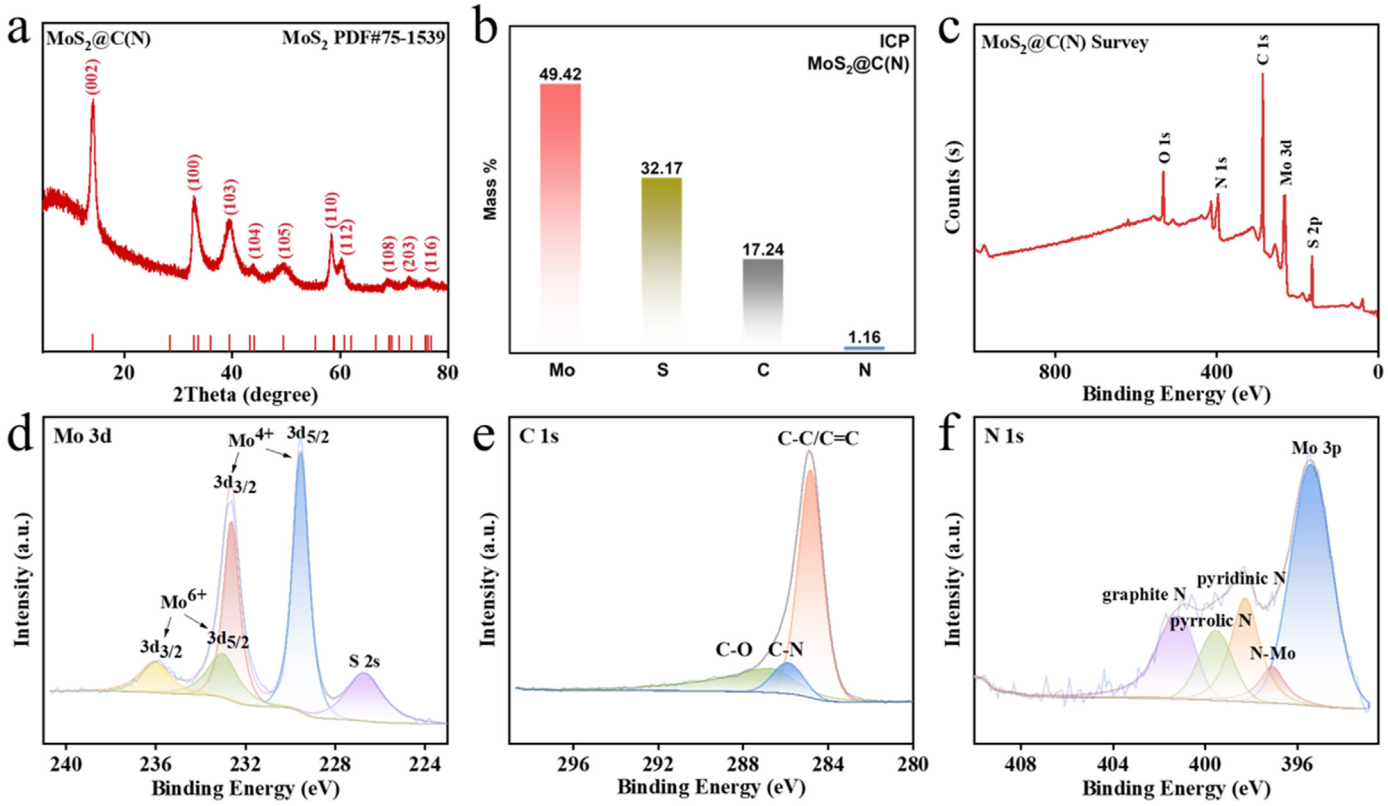

Fig. 6. (a) X-ray diffraction (XRD) pattern of the MoS_2@C(N) material, (b) element content in MoS_2@C(N) as determined by inductively coupled plasma emission spectrometry (ICP), (c) X-ray photoelectron spectroscopy (XPS) survey spectrum of MoS_2@C(N), (d) Mo 3*d* XPS spectrum, (e) C 1*s* XPS spectrum and (f) N 1*s* XPS spectrum.

For further structural analysis of the materials, Fig. 6a displays the XRD pattern of the MoS_2@C(N) composite material, where typical diffraction peaks at 14.1°, 32.9°, 39.5°, 58.8°, and 60.8° correspond to the (002), (100), (103), (110), and (112) planes of MoS_2 phase (PDF# 75–1539). The coating of the N-doped carbon layer does not alter the crystal structure of MoS_2 and its predominant crystal facets (the XRD spectrum of MoS_2 is shown in Fig. S1). Inductively coupled plasma optical emission spectrometry (ICP-OES) determined the elemental content in MoS_2@C(N) (Fig. 6b), establishing the chemical composition ratio between the surface and the entire structure. The mass percentages of Mo, S, C, and N elements are 49.42 %, 32.17 %, 17.24 %, and 1.16 %, respectively, indicating that the mass fraction of MoS_2 in the composite is 81.59 %. The low carbon content further supports the presence of the thin carbon layer. Typical XPS is employed to elucidate the bonding states and chemical composition of the sample. The XPS survey spectrum indicates that MoS_2@C(N) is mainly composed of O, N, C, Mo, and S elements (Fig. 6c), where the Mo 3*d* core level peaks are assigned to Mo^{4+} $3d_{5/2}$ (229.5 eV) and Mo^{4+} $3d_{3/2}$ (232.6 eV), and the double peaks at 233.0 eV and 236.1 eV are attributed to Mo^{6+}, the presence of them can be attributed to surface oxidation of MoS_2 [18]. Additionally, a single peak at 226.6 eV in the Mo 3*d* XPS region is observed for S 2*s* (Fig. 6d). In the S 2*p* XPS spectrum (Fig. S2), peaks at 162.3 eV for S $2p_{3/2}$ and 163.5 eV for S $2p_{1/2}$ reveal the presence of Mo−S bonds in MoS_2 with S^{2-}, while the satellite peak at 168.7 eV corresponds to surface-adsorbed sulfur oxide. In the C 1*s* spectrum (Fig. 6e), three main peaks at 284.8 eV, 285.9 eV, and 286.6 eV correspond to the C−C, C−N, and C−O bonds, respectively, indicating that the C elements in the coating layer are primarily sp^3-hybridized carbon, with successful N doped into the surface carbon layer. In the N 1*s* spectrum (Fig. 6f), a peak at 395.4 eV for Mo 3*p* and a weaker peak at 397.1 eV corresponding to Mo−N bonds demonstrate partial N doped into MoS_2, bonding with metallic Mo. Peaks at 398.3 eV, 399.5 eV, and 401.1 eV correspond to pyridinic nitrogen, pyrrolic nitrogen, and graphitic nitrogen, respectively. Pyridinic and pyrrolic nitrogen can enhance the adsorption capacity of doped materials for ions, and abundant nitrogen doping can provide more active sites for metal cations by enhancing material polarity, improving material electronic conductivity, and enhancing its electrochemical kinetic performance [19].

The mechanism of which N-doped carbon layers enhance the electrochemical performance of MoS_2 has been studied through various electrochemical and non-electrochemical testing techniques. Compared to MoS_2, the introduction of the nitrogen-doped carbon layer can significantly improve the wettability of the electrode material with the electrolyte, with the contact angle decreasing from 43.1° to 27.3° (Fig. 7a). The fitting spectra of MoS_2 and MoS_2@C(N) in terms of EIS are shown in Fig. 7b to investigate the conductivity and electrochemical kinetics of the electrodes before and after cycling. The charge transfer resistance is evaluated from the diameter of the semicircle in the high-frequency region, which describes the ease of electron transfer during redox reactions. The ion diffusion resistance is described by the slope of the straight line in the low-frequency region, and the intercept of the high-frequency region curve represents the internal resistance of the battery [20,21]. The internal figure illustrates the equivalent circuit diagram of the fitting process, where R_s is the electrolyte resistance, R_{ct} is the charge transfer resistance at the interface, and W1 is the Warburg impedance for lithium-ion diffusion process. CPE1 is the constant phase element of the corresponding capacitance. The charge transfer resistances (R_{ct}) of MoS_2 and MoS_2@C(N) are 175.4 and 94.66 Ω, respectively. This can be attributed to the introduction of the carbon layer structure, effectively enhancing the electron transfer capability on the surface of the electrode and enhancement of Li^+ adsorption capacity. After cycling, both MoS_2 and MoS_2@C(N) experience a decrease in R_{ct} to varying degrees, which can be attributed to changes in ion concentration in the electrolyte and electrode interface [21]. The R_{ct} of MoS_2@C(N)

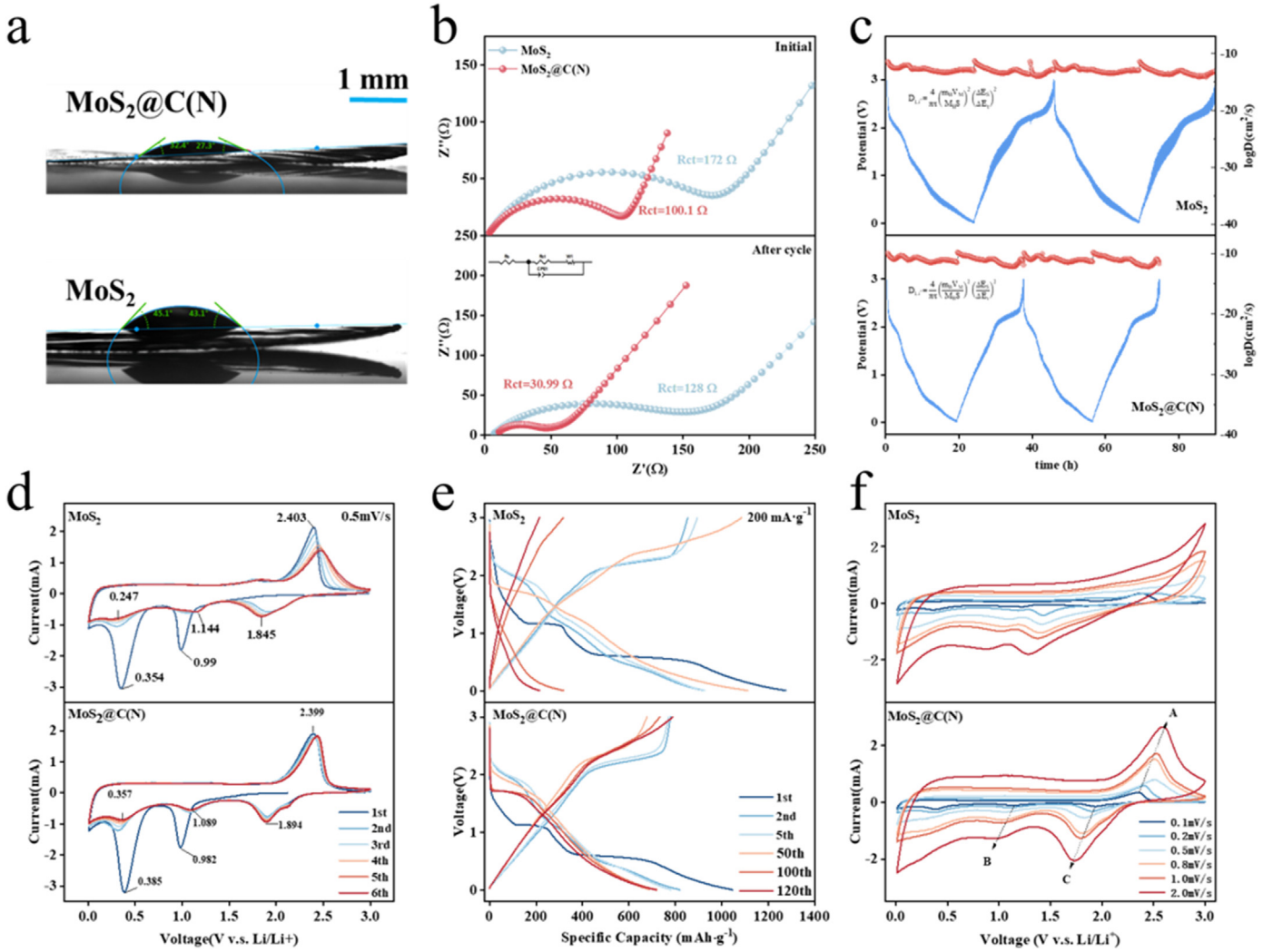

Fig. 7. (a) Contact angle between MoS_2 and MoS_2@C(N) and the electrolyte. (b) Electrochemical Impedance Spectroscopy (EIS) fitting spectra of MoS_2 and MoS_2@C(N) before and after cycling. (c) Galvanostatic Intermittent Titration Technique (GITT) curves and lithium diffusion coefficient (D_{Li^+}) for MoS_2 and MoS_2@C(N). (d) Cyclic voltammetry (CV) curves for the first six cycles at a scan rate of 0.5 mV $s^{-1}$of MoS_2 and MoS_2@C(N). (e) Specific capacity-voltage curves of MoS_2 and MoS_2@C(N) at a current density of 200 mA g^{-1}. (f) CV curves at different scan rates of MoS_2 and MoS_2@C(N).

decreases to 29.34 Ω. Under the same conditions, MoS_2 decreases to 116.9 Ω, indicating a significant improvement in the infiltration effect of the electrolyte due to the presence of loose carbon layers.

Furthermore, the actual diffusion coefficient of Li^+ during the cycling process was also obtained using GITT. The GITT results include the influence of diffusion kinetics during the insertion/extraction processes. Fig. S3 shows the GITT curves for the first cycle (Fig. S3a) and the 50th cycle (Fig. S3b). When E is linearly related to $\tau^{1/2}$, the simplified Eq. (S1) can be used to calculate the D_{Li^+} of the material [22]. The calculated results are shown in Fig. 7c. Since the contribution of side reactions such as electrolyte decomposition to the capacity is very small, all capacities in this study are directly attributed to the extraction and re-insertion of lithium ions in MoS_2@C(N). The value of D_{Li^+} varies significantly within the range from 10^{-10} to 10^{-11} cm^2 s^{-1} with different electrode states. Similar to previous reports, the initial D_{Li^+} is very high at the beginning of discharge; then, as Li^+ is inserted, this value slightly decreases and remains at a relatively high level. The charging process exhibits a similar trend to the discharge process, which is related to the changes in material composition and structure caused by Li^+ extraction [22,23]. The D_{Li^+} of MoS_2 (Fig. 7c) shows similar variations to MoS_2@C(N), but D_{Li^+} ranges from 10^{-11} to 10^{-14} cm^2 s^{-1}, significantly lower than that of MoS_2@C(N). This can be attributed to the improvement of the electronic structure of MoS_2 and the ion migration path by the introduction of the nitrogen-doped carbon layer.

The CV curves were employed to evaluate the lithium storage behavior of the electrode. Fig. 7d illustrates the CV curves of MoS_2 and MoS_2@C(N) for the first six cycles at a scan rate of 0.5 mV s^{-1}. In the initial scan, irreversible reduction peaks around 0.385 V and 0.982 V are attributed to electrolyte decomposition and the formation of solid electrolyte interface (SEI) [24,25]. In the second cycle, the peak at 1.894 V corresponds to the formation of Li_xMoS_2 intercalation compounds and the subsequent 2H to 1T phase transition (Fig. S4), while the peak at 1.089 V arises from further conversion of Li_xMoS_2 to metallic Mo and Li_2S, as indicated by Eq. (S2) in the Supplementary data [9,26,27]. During the reverse scan, the oxidation peak around 2.399 V mainly originates from the oxidation of Li_2S to S. The absence of other obvious oxidation peaks indicates minimal oxidation of metallic Mo to MoS_2. In subsequent cycles, owing to the introduction of nitrogen-doped carbon covalently coupled structure, better overlap of CV curves is observed, indicating high reversibility and stability of the MoS_2@C(N) electrode during charge-discharge processes.

Fig. 7e presents the charge-discharge curves of MoS_2 and MoS_2@C(N) electrode for the 1st, 2nd, 5th, 50th, 100th, and 120th cycles at a current density of 200 mA g^{-1}. Within the voltage range of 0.01–3V at room

temperature, the initial discharge specific capacity reaches 1045 mAh g^{-1}, followed by 818.5 mAh g^{-1} for the 2nd cycle, with a coulombic efficiency of 95.3 %. Even after 120 cycles, a high specific capacity of 716 mAh g^{-1} is maintained. In comparison, the MoS_2 electrode exhibits rapid capacity decay under the same testing conditions, with an initial discharge specific capacity of 1275.6 mAh g^{-1}, dropping to 923.8 mAh g^{-1} for the 2nd cycle and further decreasing to 215.3 mAh g^{-1} after 120 cycles. The significant enhancement in cycling stability can be attributed to the alleviation of volume expansion during the lithiation/de-lithiation process and the improvement in conductivity of MoS_2 facilitated by the loose carbon layer structure.

Fig. 7f presents the CV curves of MoS_2@C(N) material at different scan rates during lithium storage, showing that the CV curves obtained at different scan rates are basically similar, indicating minimal polarization of the electrode material. Additionally, with scan rate increasing, the cathodic oxidation peak shifts towards positive potential and the anodic reduction peak shifts towards negative potential, attributed to the increase of internal resistance of the electrode [28]. The *b* values can be determined as a function of log *i* and log *v* in Fig. S5. When the *b* value approaches 0.5, the electrochemical behavior is primarily controlled by diffusion mechanisms. When the *b* value approaches 1, the electrochemical behavior is primarily controlled by capacitance [29]. The *b* values at oxidation peak A, reduction peak B, and peak C are 0.687, 0.820, and 0.880, respectively, indicating that the electrode material simultaneously exhibits pseudocapacitive and diffusion-controlled processes, with capacitive processes predominantly contributing to charge storage. Furthermore, the ratio of capacitance contribution to diffusion contribution is shown in Fig. S6. At scan rates of 0.1 mV s^{-1}, 0.2 mV s^{-1}, 0.5 mV s^{-1}, 0.8 mV s^{-1}, 1.0 mV s^{-1}, and 2.0 mV s^{-1}, the materials exhibit pseudocapacitive contribution rates of 58.92 %, 62.09 %, 65.79 %, 72.21 %, 76.34 %, and 88.18 %, respectively. The ratio of capacitance contribution increases with increasing scan rate. The enhanced capacitance-controlled behavior can be attributed to the synergistic effect of nitrogen-doped carbon layer and MoS_2 nanoparticles [29,30]. Interconnected loose carbon layers effectively improve the conductivity of MoS_2 nanoparticles and enhance the contact between the electrode and the electrolyte.

To further elucidate the influence of the constructed N-doped carbon layer on the cycling stability of MoS_2 electrode materials, the anomalous SEM images and particle size analysis of MoS_2 and MoS_2@C(N) electrodes were tested before cycling, after 1 cycle, and after 25 cycles (Fig. 8a and Fig. S7). With the progression of charge-discharge cycling,

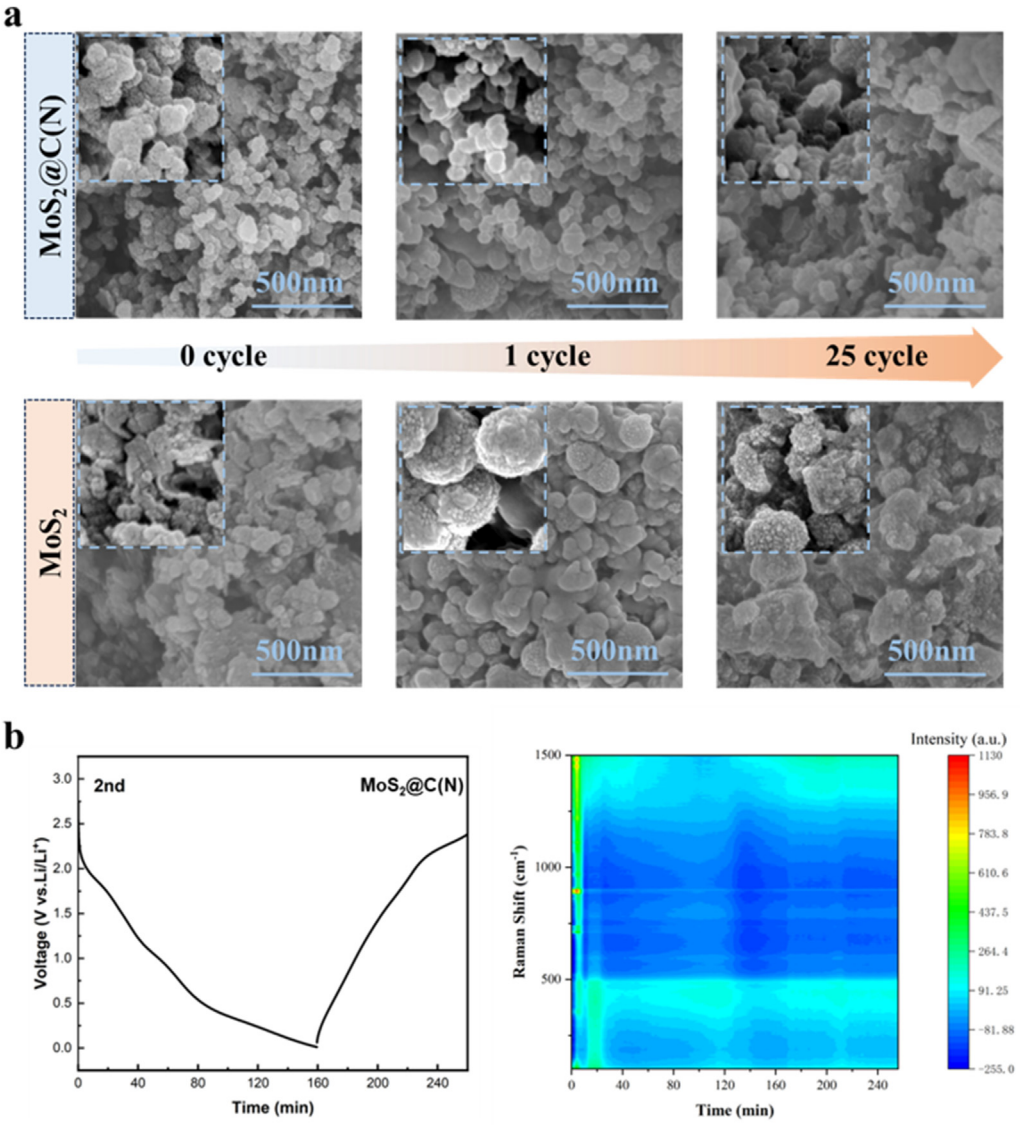

Fig. 8. (a) SEM images and particle size analysis of MoS_2 and MoS_2@C(N) electrode after standing in electrolyte, followed by 1 cycle and 25 cycles. (b) The time-voltage curve and *in situ* Raman spectra of MoS_2@C(N) during the second cycle.

irreversible desorption of some Li^+ leads to changes in the size of active particles and varying degrees of particle aggregation. This phenomenon may contribute to the initial capacity decay during cycling. Compared to MoS_2, the MoS_2@C(N) electrode benefits from the constraining effect of the N-doped carbon layer, exhibiting lesser particle aggregation and size variation, consistent with its higher cycling stability. Additionally, the reaction mechanism of MoS_2@C(N) electrode during lithiation-de-lithiation was analyzed using *in situ* Raman spectroscopy. MoS_2 exhibits two strong peaks at ~383 cm^{-1} and ~408 cm^{-1}. During lithiation, the intensity of these peaks gradually decreases due to the conversion reactions between Li_xMoS_2 and MoS_2 compounds forming Li_2S and Mo [Eq. (S2)]. As the de-lithiation process proceeds, the intensity of the peaks gradually recovers, demonstrating the structural stability of MoS_2@C(N) during its lithium storage process (Fig. 8b) [31].

Fig. 9a illustrates the cycling performance of MoS_2 and MoS_2@C(N) electrodes at a current density of 500 mA g^{-1}. After 200 cycles, the capacity of MoS_2 significantly declines to only 235.3 mAh g^{-1}, with a capacity retention rate of only 32.4 %. In contrast, MoS_2@C(N) exhibits a specific capacity of 753.9 mAh g^{-1} with a high capacity retention rate of 92.2 %. Fig. 9b evaluates the rate performance of MoS_2 and MoS_2@C(N) electrodes within the current density range of 100–5000 mA g^{-1}. As the current density increases from 100 mA g^{-1} to 200, 500, 800, 1000, 2000, and 5000 mA g^{-1}, the corresponding average discharge specific capacities decrease from 846 mAh g^{-1} to 792.2, 744.4, 673.4, 612.1, 562.1.5, and 480.3 mAh g^{-1}, respectively. Reverting to a current density of 100 mA g^{-1}, the battery's specific capacity rapidly recovers and remains stable at 824.9 mAh g^{-1}, with a coulombic efficiency of 98 %, indicating excellent reversibility and superior rate capability of the MoS_2@C(N) electrode. This can be attributed to the uniform distribution of three-dimensional channels within the material, which shortens the ion diffusion path, enhances the electron and ion migration rates, and thus achieves high-rate capacity. It is noteworthy that at a current density of 5000 mA g^{-1}, the specific capacity of MoS_2 declines rapidly due to the lack of a structured coating layer for protection, leading to the destruction of the internal structure and loss of stable lithium storage capability. In contrast, the MoS_2@C(N) electrode maintains a specific capacity of 302.9 mAh g^{-1} after 500 cycles, demonstrating stable lithium storage capability. The material's strong rate performance and high stability indicate the decisive influence of the carbon layer on the electrochemical stability of MoS_2.

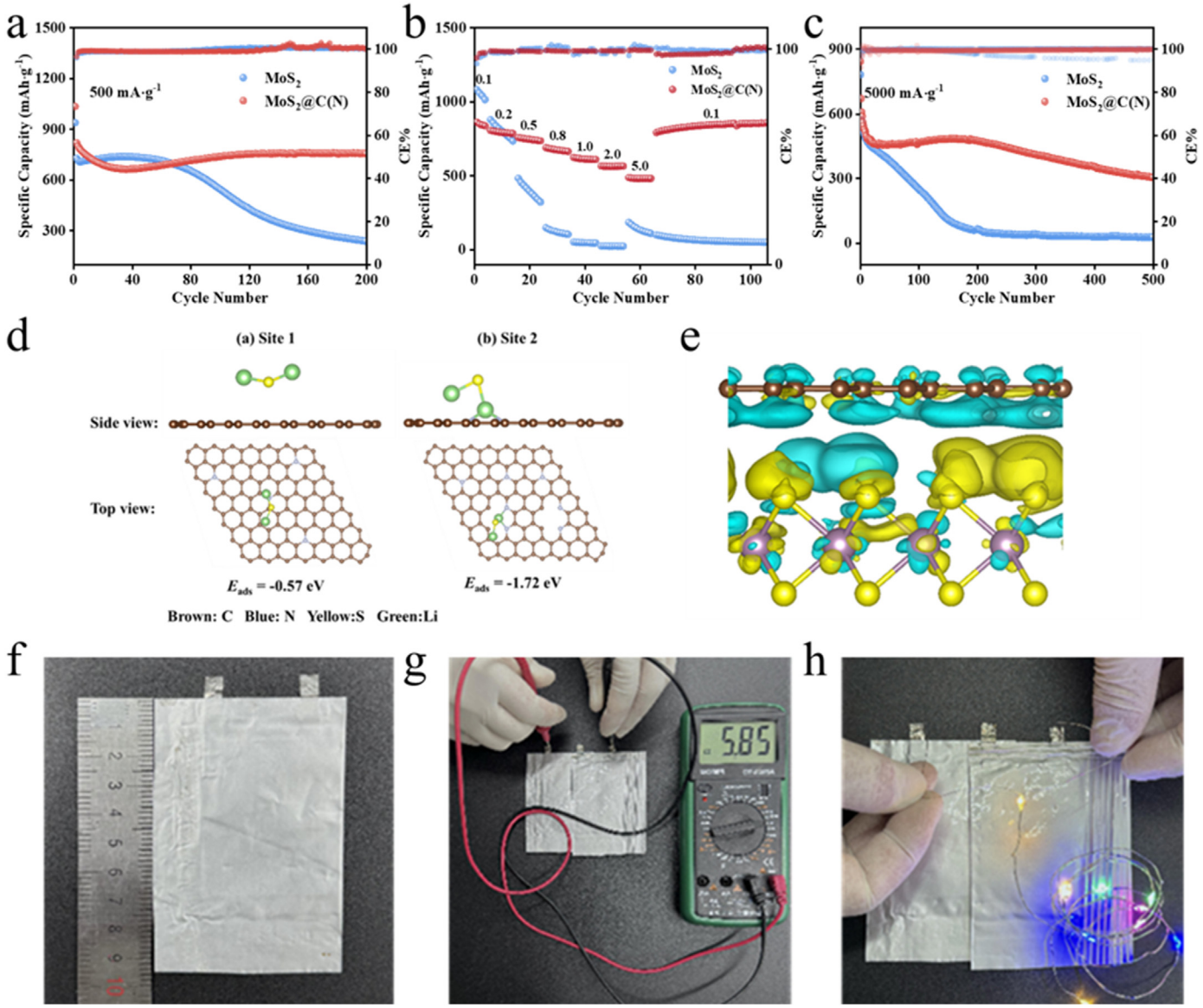

Fig. 9. Charge-discharge cyclic curves for MoS_2 and MoS_2@C(N) at (a) a current density of 500 mA g^{-1} and (b) rate performance. (c) Charge-discharge cyclic curves at a current density of 5000 mA g^{-1}. (d) Dimensions of the pouch full cell. (e) Series voltage of series pouch full cell and (f) the picture of battery light device.

In situ polymerization of chain-like Schiff base polymers under ultrasound conditions results in their uniform distribution on the surface of MoS_2 particles, leading to a relatively even distribution of nitrogen-doped carbon layers after carbonization. Meanwhile, nitrogen atoms mainly exist in the form of pyridinic nitrogen and pyrrolic nitrogen. Therefore, density functional theory (DFT) calculations were employed to study the adsorption energy of Li_2S on nitrogen-doped carbon networks with different doping types. Using PWSCF software, the binding energies (E_{ads}) of Li_2S with nitrogen-doped carbon networks in two different distribution states were obtained. As shown in Fig. 9d, compared to the unevenly distributed graphitic nitrogen ($E_{ads} = -0.57$ eV), the relatively evenly distributed pyrrolic nitrogen and pyridinic nitrogen ($E_{ads} = -1.72$ eV) exhibit higher adsorption capacity for Li_2S. This suggests that nitrogen atoms uniformly doped in the conjugated carbon network can effectively suppress the dissolution of Li_2S. Fig. 9e displays the differential charge density iso-surface of MoS_2@C(N), where the yellow area represents the electron-enriched region, and the cyan area represents the electron-deficient region. Differential charge density analysis indicates a significant electronic rearrangement at the interface between MoS_2 and the nitrogen-doped carbon network, accelerating the charge transfer kinetics. The denser distribution of deformed charges between interface atoms suggests covalent bonding between the two phases. The change in electron density affects the adsorption of reactants and intermediates on active sites, particularly the nitrogen atoms rich in electrons at the interface, which facilitate the adsorption of Li_2S.

To further explore the application value of MoS_2@C(N), MoS_2@C(N)||$LiPF_6$/EC/DEC||LFP pouch cells were assembled after pre-lithiation (Fig. 9f–h). After charging to 3.2 V and resting for 6 h, two pouch cells were connected in series, maintaining a voltage of 5.85 V, successfully powering a device consisting of 9 LED lights connected in series.

In addition, the advantages of modification strategies in the sodium-ion storage process have also been studied to evaluate their impact on ion accommodation capacity through adjustments in surface electronic structure. As shown in Fig. S8, under the same current density, the MoS_2@C(N) electrode exhibits significantly higher capacity performance. At the current densities of 50, 100, 200, 500, and 1000 mA g^{-1}, the discharge specific capacities are 445, 320, 235, 148, and 36 mAh g^{-1}, respectively. Thanks to the maintenance of the active material structure, when the current is restored to 100 mA g^{-1}, the specific capacity of MoS_2@C(N) is well restored, averaging 227 mAh g^{-1}. Fig. S9 shows the specific capacity-voltage curves of MoS_2 and MoS_2@C(N) within the voltage range of 0.01–2.5 V. The initial discharge specific capacity of the MoS_2@C(N) electrode is 667.15 mAh g^{-1}, and the subsequent charge-discharge curves show good overlap, which can be attributed to the carbon layer coating inhibiting the volume changes of MoS_2 caused by the repeated insertion and extraction of Na^+. Fig. S10 records the cycling performance of the electrodes at 50 mA g^{-1} and 500 mA g^{-1}, respectively. Under a low current density of 50 mA g^{-1}, after 100 cycles, the specific capacity of MoS_2 rapidly decreased, with a capacity retention rate of only 45.5 %; whereas the specific capacity of MoS_2@C(N) changed more stably, with a sodium storage specific capacity of 298.5 mAh g^{-1} after 100 cycles, a coulombic efficiency close to 100 %, and a capacity retention rate increased to 71 %. At a high current density of 500 mA g^{-1}, after repeated charge and discharge for 300 cycles, the specific capacity of MoS_2@C(N) is 202 mAh g^{-1}, with a nearly 100 % coulombic efficiency. In contrast, the specific capacity of MoS_2 is less than 20 mAh g^{-1}.

4. Conclusion

In summary, according to the theoretical calculation results, the ion transport kinetics and cyclic stability of commercial MoS_2 have been improved through mechanical pulverization and N-doped carbon layer coating achieved by high-energy ball milling, ultrasound-assisted *in situ* coating and carbonization. Benefiting from the synergistic effects of elemental and structural modifications, the MoS_2/C(N) electrode exhibits excellent lithium storage performance as an anode material for LIBs, with a specific capacity of 753.9 mAh g^{-1} after 200 cycles at a current density of 500 mA g^{-1}, and a capacity retention percentage of 92.2 %. Even at a high current density of 5 A g^{-1}, it retains a specific capacity of 302.9 mAh g^{-1} after 500 cycles. Experimental validation and theoretical calculations indicate that the N-doped carbon layer significantly enhances the electrochemical performance of commercial MoS_2, showcasing its vast potential for future applications in lithium-ion batteries.

CRediT authorship contribution statement

Ning Zhang: Writing – original draft, Methodology, Investigation, Conceptualization. **Yuetong Li:** Writing – original draft, Methodology, Investigation, Conceptualization. **Botao Zhang:** Methodology, Investigation. **Shengyu Gao:** Methodology, Investigation. **Yongxin Huang:** Writing – review & editing, Resources, Conceptualization. **Li Li:** Writing – review & editing, Conceptualization. **Feng Wu:** Writing – review & editing, Conceptualization. **Renjie Chen:** Writing – review & editing, Resources, Conceptualization.

Declaration of competing interest

The authors declare that they have no known competing financial interests or personal relationships that could have appeared to influence the work reported in this paper.

Acknowledgements

This work was supported by the Joint Funds of the National Natural Science Foundation of China (U2130204), the Young Elite Scientists Sponsorship Program by CAST (YESS20200364), Beijing Outstanding Young Scientists Program (BJJWZYJH01201910007023), and the Fundamental Research Funds for the Central Universities (2024CX06107).

Appendix A. Supplementary data

Supplementary data to this article can be found online at https://doi.org/10.1016/j.tramat.2025.100013.

References

[1] M. Li, J. Lu, Z. Chen, K. Amine, 30 years of lithium-ion batteries, Adv. Mater. 30 (2018) 1800561, https://doi.org/10.1002/adma.201800561.
[2] T. Kim, W. Song, D.-Y. Son, L.K. Ono, Y. Qi, Lithium-ion batteries: outlook on present, future, and hybridized technologies, J. Mater. Chem. A 7 (2019) 2942–2964, https://doi.org/10.1039/C8TA10513H.
[3] J. Xu, X. Cai, S. Cai, Y. Shao, C. Hu, S. Lu, S. Ding, High-energy lithium-ion batteries: recent progress and a promising future in applications, Energy Environ. Mater. 6 (2023) e12450, https://doi.org/10.1002/eem2.12450.
[4] H. Cheng, J.G. Shapter, Y. Li, G. Gao, Recent progress of advanced anode materials of lithium-ion batteries, J. Energy Chem. 57 (2021) 451–468, https://doi.org/10.1016/j.jechem.2020.08.056.
[5] P. Nzereogu, A. Omah, F. Ezema, E. Iwuoha, A. Nwanya, Anode materials for lithium-ion batteries: a review, Appl. Surf. Sci. Adv. 9 (2022) 100233, https://doi.org/10.1016/j.apsadv.2022.100233.
[6] Q. Wang, B. Liu, Y. Shen, J. Wu, Z. Zhao, C. Zhong, W. Hu, Confronting the challenges in lithium anodes for lithium metal batteries, Adv. Sci. 8 (2021) 2101111, https://doi.org/10.1002/advs.202101111.
[7] D.-H. Liu, Z. Bai, M. Li, A. Yu, D. Luo, W. Liu, L. Yang, J. Lu, K. Amine, Z. Chen, Developing high safety Li-metal anodes for future high-energy Li-metal batteries: strategies and perspectives, Chem. Soc. Rev. 49 (2020) 5407–5445, https://doi.org/10.1039/C9CS00636B.
[8] S. Wang, C. Qu, C. Wang, J. Wen, X. Ma, Y. Yang, H. Sun, S. Xu, G. Huang, Progress of transition metal sulfides used as the lithium-ion battery anodes, Mater. Chem. Front. 7 (2023) 2779–2808, https://doi.org/10.1039/D2QM01200F.
[9] L. Zhao, Y. Wang, C. Wei, X. Huang, X. Zhang, G. Wen, MoS_2-based anode materials for lithium-ion batteries: developments and perspectives, Particuology 87 (2024) 240–270, https://doi.org/10.1016/j.partic.2023.08.009.

[10] C. Liu, Y. Bai, Y. Zhao, H. Yao, H. Pang, MoS_2/graphene composites: fabrication and electrochemical energy storage, Energy Storage Mater. 33 (2020) 470–502, https://doi.org/10.1016/j.ensm.2020.06.020.
[11] Y. Wu, Y. Yu, 2D material as anode for sodium ion batteries: recent progress and perspectives, Energy Storage Mater. 16 (2019) 323–343, https://doi.org/10.1016/j.ensm.2018.05.026.
[12] Y. Zhou, Q. Li, Q. Han, L. Zhao, Y. Liu, Y. Wang, Z. Li, C. Dong, X. Sun, J. Yang, X. Zhang, F. Jiang, Design of high-capacity MoS_3 decorated nitrogen doped carbon coated Cu_2S electrode structures with dual heterogenous interfaces for outstanding sodium-ion storage, Small 19 (2023) 2303742, https://doi.org/10.1002/smll.202303742.
[13] W.J. Lee, J. Lim, S.O. Kim, Nitrogen dopants in carbon nanomaterials: defects or a new opportunity? Small Methods 1 (2017) 1600014 https://doi.org/10.1002/smtd.201600014.
[14] Z. Zhang, X. Lin, S. Tang, H. Xie, Q. Huang, Self-supported system of MoO_2@ Ni_2P heterostructures as an efficient electrocatalyst for hydrogen evolution reactions in alkaline media, J. Colloid Interface Sci. 630 (2023) 494–501, https://doi.org/10.1016/j.jcis.2022.10.041.
[15] Y. He, J. Sun, W. Yao, K. Lu, D. Liu, H. Xie, C. Huang, N. Jia, A self-powered photoelectrochemical molecular imprinted sensor for chloroquine phosphate with enhanced cathodic photocurrent via stepped energy band alignment engineering, Chem. Eng. J. 451 (2023) 138748, https://doi.org/10.1016/j.cej.2022.138748.
[16] W. Sun, X. Tang, Q. Yang, Y. Xu, F. Wu, S. Guo, Y. Zhang, M. Wu, Y. Wang, Coordination-induced interlinked covalent-and metal-organic-framework hybrids for enhanced lithium storage, Adv. Mater. 31 (2019) 1903176, https://doi.org/10.1002/adma.201903176.
[17] L. Fu, H. Liu, C. Li, Y. Wu, E. Rahm, R. Holze, H. Wu, Surface modifications of electrode materials for lithium ion batteries, Solid State Sci. 8 (2006) 113–128, https://doi.org/10.1016/j.solidstatesciences.2005.10.019.
[18] J.-G. Wang, H. Liu, R. Zhou, X. Liu, B. Wei, Onion-like nanospheres organized by carbon encapsulated few-layer MoS_2 nanosheets with enhanced lithium storage performance, J. Power Sources 413 (2019) 327–333, https://doi.org/10.1016/j.jpowsour.2018.12.055.
[19] S. Sahoo, C.S. Rout, Facile electrochemical synthesis of porous manganese-cobalt-sulfide based ternary transition metal sulfide nanosheets architectures for high performance energy storage applications, Electrochim. Acta 220 (2016) 57–66, https://doi.org/10.1016/j.electacta.2016.10.043.
[20] C. Deng, H. Wang, S. Wang, Clarifying the lithium storage behavior of MoS_2 with *in situ* electrochemical impedance spectroscopy, J. Mater. Chem. A 9 (2021) 15734–15743, https://doi.org/10.1039/D1TA02517A.
[21] D. He, Y. Yang, Z. Liu, J. Shao, J. Wu, S. Wang, L. Shen, N. Bao, Solvothermal-assisted assembly of MoS_2 nanocages on graphene sheets to enhance the electrochemical performance of lithium-ion battery, Nano Res. 13 (2020) 1029–1034, https://doi.org/10.1007/s12274-020-2739-3.
[22] A. Nickol, T. Schied, C. Heubner, M. Schneider, A. Michaelis, M. Bobeth, G. Cuniberti, GITT analysis of lithium insertion cathodes for determining the lithium diffusion coefficient at low temperature: challenges and pitfalls, J. Electrochem. Soc. 167 (2020) 090546, https://doi.org/10.1149/1945-7111/ab9404.
[23] C. Hong, Q. Leng, J. Zhu, S. Zheng, H. He, Y. Li, R. Liu, J. Wan, Y. Yang, Revealing the correlation between structural evolution and Li^+ diffusion kinetics of nickel-rich cathode materials in Li-ion batteries, J. Mater. Chem. A 8 (2020) 8540–8547, https://doi.org/10.1039/D0TA00555J.
[24] Y. Yang, R. Dong, H. Cheng, L. Wang, J. Tu, S. Zhang, S. Zhao, B. Zhang, H. Pan, Y. Lu, 2D layered materials for fast-charging lithium-ion battery anodes, Small 19 (2023) 2301574, https://doi.org/10.1002/smll.202301574.
[25] P. Ge, L. Zhang, Y. Yang, W. Sun, Y. Hu, X. Ji, Advanced $MoSe_2$/carbon electrodes in Li/Na-ions batteries, Adv. Mater. Interfac. 7 (2020) 1901651, https://doi.org/10.1002/admi.201901651.
[26] C. Sun, M. Liu, L. Wang, L. Xie, W. Zhao, J. Li, S. Liu, D. Yan, Q. Zhao, Revisiting lithium-storage mechanisms of molybdenum disulfide, Chin. Chem. Lett. 33 (2022) 1779–1797, https://doi.org/10.1016/j.cclet.2021.08.052.
[27] W. Zhu, J. Zhao, X. Tao, MoS_2-carbon based nanocomposites as anodes for lithium-ion batteries: a review, J. Energy Storage 84 (2024) 110934, https://doi.org/10.1016/j.est.2024.110934.
[28] G. Wang, X. Leng, S. Han, Y. Shao, S. Wei, Y. Liu, J. Lian, Q. Jiang, How to improve the stability and rate performance of lithium-ion batteries with transition metal oxide anodes, J. Mater. Res. 32 (2017) 16–36, https://doi.org/10.1557/jmr.2016.330.
[29] M. Cao, Y. Feng, P. Zhang, L. Yang, X. Gu, J. Yao, Synthesis of MoS_2 nanotube using a sacrificial template method as advanced anode material for lithium-ion batteries, J. Alloys Compd. 907 (2022) 164499, https://doi.org/10.1016/j.jallcom.2022.164499.
[30] X. Li, R. Wang, Q. Wu, Y. Yu, T. Gao, T. Yao, X. Wang, J. Han, B. Song, Synergistically designed dual interfaces to enhance the electrochemical performance of MoO_2/MoS_2 in Na-and Li-ion batteries, Small 19 (2023) 2206940, https://doi.org/10.1002/smll.202206940.
[31] F. Xiong, H. Wang, X. Liu, J. Sun, M. Brongersma, E. Pop, Y. Cui, Li intercalation in MoS_2: *in situ* observation of its dynamics and tuning optical and electrical properties, Nano Lett. 15 (2015) 6777–6784. https://pubs.acs.org/doi/abs/10.1021/acs.nanolett.5b02619.